Density Field Dynamics and Its Variant Extensions: A Constrained Flat-Background Optical-Medium Family

Gary Thomas Alcock

October 2, 2025

Abstract

We present Density Field Dynamics (DFD), a flat-background optical-medium framework that is both fully consistent with existing tests of general relativity and falsifiable by upcoming laboratory experiments. DFD reproduces all standard solar-system and weak-field post-Newtonian predictions, while yielding two decisive laboratory discriminators: (1) non-null cavity–atom frequency *slopes* across gravitational potential differences, and (2) a T^3 contribution to matter-wave interferometer phases. The framework is defined by a scalar refractive index $n = e^{\psi}$ that controls both light propagation and inertial dynamics; we provide explicit field equations, recover Newtonian and post-Newtonian limits, and derive quantitative forms of the laboratory discriminators. We then map six bounded extensions—electromagnetic back-reaction, dual-sector (ϵ/μ) splitting, nonlocal kernels, vector anisotropy, stochasticity, and strong-field closure variants—which address specific anomalies while reducing to the same base framework. Beyond the laboratory and solar system, we incorporate an embedded transverse–traceless (TT) spin-2 sector with $c_T = 1$ and GR polarizations, reproduce black-hole/shadow observables via optical geodesics of $n = e^{\psi}$, and develop a minimal cosmology module yielding concrete distance biases and H_0 anisotropies. **Thus DFD is simultaneously conservative (matching GR where tested) and falsifiable (predicting distinctive, testable departures), with a complete observational coverage from laboratory clocks to gravitational waves, black holes, and cosmology.**

1 Introduction

Einstein's general relativity (GR) geometrizes gravitation as spacetime curvature. Yet alternatives remain viable, from scalar–tensor theories [1] to $f(R)$ models [2] and Einstein–æther theories [3]. If one restricts attention to flat Minkowski spacetime while maintaining an invariant two-way light speed, then a natural minimal class emerges: *refractive* or *optical-medium* theories, where gravity manifests through a scalar index field controlling rods, clocks, and phases. This aligns with scalar frameworks [5, 6] and analog-gravity constructions [4].

The motivation for DFD is not metaphysical elegance but *experimental falsifiability.* Two sharp discriminators appear immediately:

1. **Cavity–atom Local Position Invariance (LPI) slope:** GR predicts a strict null in the *ratio* of cavity to atomic frequencies across potential differences (within standard PPN and composition-independence assumptions [8, 7, 9, 25]). DFD predicts a non-null slope under operational conditions defined below ("nondispersive band"), sharpened in the dual-sector extension.

2. **Matter-wave interferometry:** DFD predicts a small but testable T^3 contribution to the phase, absent in GR at leading order.

*Finally, we provide concise but quantitative predictions in the remaining sectors—*gravitational waves *(embedded TT spin-2 with $c_T = 1$),* black holes/shadows *(optical geodesics), and* cosmology *(distance bias and H_0 anisotropy)—so the proposal is complete across observational domains.*

2 Base Density Field Dynamics

2.1 Field equations

DFD postulates a scalar refractive field ψ such that

$$n = e^{\psi}, \tag{1}$$

so that geometric optics is governed by Fermat's principle in n, while matter accelerates according to

$$\mathbf{a} = \tfrac{c^2}{2}\,\nabla\psi. \tag{2}$$

General sourcing law (global). Allowing a single crossover function μ between high-gradient (solar) and deep-field (galactic) regimes, the scalar obeys

$$\nabla\cdot\Big[\mu\big(|\nabla\psi|/a_\star\big)\,\nabla\psi\Big] = -\,\frac{8\pi G}{c^2}\,(\rho-\bar\rho), \tag{3}$$

with $\mu\!\to\!1$ in the solar/high-gradient regime and $\mu(x)\!\sim\!x$ in the deep-field regime.

Local reduction (solar/laboratory). In laboratory and solar-system applications, $\mu \to 1$ and the uniform background $\bar\rho$ contributes only a constant offset to ψ that drops out of local gradients; thus

$$\nabla^2\psi = \frac{8\pi G}{c^2}\,\rho, \tag{4}$$

so that $\psi = 2\Phi/c^2$ with Φ the Newtonian potential. Equation (4) is the local, Poisson-like sourcing law; the nonlocal kernel variant generalizes this, and Eq. (3) governs deep-field/cosmological optics.

2.2 Weak-field predictions

From (4) one recovers:

- **Newtonian limit:** $\mathbf{a} = -\nabla\Phi$.
- **Gravitational redshift:** $\Delta f/f = \Delta\Phi/c^2$.
- **Light bending:** Fermat's principle yields $\alpha = 4GM/(bc^2)$ (Appendix A), reproducing GR's factor of two.
- **Shapiro delay and perihelion precession:** match GR at 1PN order [7].
- **PPN parameters:** $\gamma = 1,\ \beta = 1$ in the standard tests, matching GR at this level [7].

2.3 Laboratory discriminators

Operationally nondispersive band (precision definition). By a *nondispersive band* we mean a frequency range $\mathcal{B}$ around the cavity/clock operating frequencies such that

$$\left|\frac{\partial n}{\partial\omega}\right|_{\mathcal{B}} \ll \frac{1}{\omega} \quad \text{and} \quad \left|\frac{\Delta n}{n}\right|_{\mathcal{B}} \lesssim \mathcal{O}(10^{-15}) \text{ over the measurement bandwidth.} \tag{5}$$

This ensures phase and group velocities coincide to the precision needed for LPI comparisons, so the cavity frequency shift tracks $n = e^{\psi}$ without dispersive contamination.

Base-DFD LPI mechanism (explicit). Within a verified nondispersive band $\mathcal{B}$, let the cavity resonance obey

$$\frac{f_{\rm cav}}{f_{\rm cav,0}} = e^{\psi}, \tag{6}$$

while the co-located atomic transition responds *operationally* as

$$\frac{f_{\rm at}}{f_{\rm at,0}} = e^{\psi'}, \tag{7}$$

where ψ' need not equal ψ (a solid's optical path and an internal atomic interval can couple differently to the scalar field in an effectively nondispersive band). The measured ratio then acquires a slope

$$\frac{f_{\rm cav}}{f_{\rm at}} = \frac{f_{\rm cav,0}}{f_{\rm at,0}}\, e^{\psi-\psi'} \quad \Rightarrow \quad \frac{\Delta(f_{\rm cav}/f_{\rm at})}{(f_{\rm cav}/f_{\rm at})} = \Delta(\psi - \psi')\,, \tag{8}$$

which is *geometry-locked* via $\Delta\Phi/c^2$ along the height change. In the dual-sector extension below, $\psi - \psi'$ becomes parametrically larger because ϵ and μ respond oppositely, sharpening the discriminator.

LPI slope test. In GR, both atoms and cavities redshift as $\Delta f/f = \Delta\Phi/c^2$, so their *ratio* is constant (strict null). In base DFD, the small difference $\psi - \psi'$ above yields a non-null ratio slope. For ground-to-satellite $\Delta\Phi \sim 5 \times 10^7$ m^2/s^2, this gives $\Delta f/f \sim 5 \times 10^{-10}$. Current ratio bounds are at $\sim 10^{-7}$ [10, 11], leaving discovery space.

Matter-wave interferometry. In addition to the GR term $\Delta\phi \sim k_{\rm eff}\, g\, T^2$, DFD predicts a T^3 correction arising from gradient variations in ψ (Appendix B). This correction is even in $k_{\rm eff}$ and rotation-odd, providing a discriminator. Estimated magnitude near Earth is $\sim 10^{-2}$ rad for $T \sim 1$ s, within reach of long-baseline interferometers and planned 10–100 m facilities [12, 13, 14, 15, 16].

3 Transverse–traceless (TT) gravitational waves within the optical ansatz

Within the same optical structure, promote the spatial sector to carry TT fluctuations,

$$g_{00} = -e^{\psi}, \qquad g_{ij} = e^{-\psi}\left(\delta_{ij} + h_{ij}^{\rm TT}\right), \quad \partial_i h_{ij}^{\rm TT} = 0, \quad h^{i}{}_{i}^{\rm TT} = 0. \tag{9}$$

Expanding the DFD scalar action to quadratic order in $h_{ij}^{\rm TT}$ yields the unique local kinetic term

$$S_{TT} = \frac{c^4}{64\pi G}\int dt\, d^3x\, \left[\tfrac{1}{c^2}(\partial_t h_{ij}^{\rm TT})^2 - (\nabla h_{ij}^{\rm TT})^2\right], \tag{10}$$

so the wave speed is $c_T = 1$. The sourced wave equation is

$$(\partial_t^2 - c^2\nabla^2)h_{ij}^{\rm TT} = \frac{16\pi G}{c^2}\left(T_{ij}^{({\rm m}),{\rm TT}} + \Pi_{ij}^{(\psi),TT}\right), \tag{11}$$

where $T_{ij}^{({\rm m}),{\rm TT}}$ is the TT projection of the matter stress and $\Pi_{ij}^{(\psi),TT}$ the near-zone ψ stress. Compact binaries therefore radiate the two GR-like quadrupolar polarizations at leading PN order with $c_T = 1$ [23, 24]. Any DFD-specific amplitude/phase corrections enter through $\Pi_{ij}^{(\psi),TT}$ and are PN-suppressed; parametrically,

$$\left.\frac{\delta h}{h}\right|_{\rm DFD} \sim \kappa_\psi \left(\frac{v}{c}\right)^4, \qquad \kappa_\psi = \mathcal{O}(1), \tag{12}$$

i.e., $\gtrsim$2PN relative to the GR quadrupole, consistent with current bounds.

4 Black holes and shadows in DFD optics

In the optical-metric viewpoint, null rays follow Fermat geodesics of $n = e^{\psi}$. For a static, spherically symmetric source with $\psi(r) = 2GM/(c^2 r)$ in the high-gradient regime, the conserved impact parameter is $b = n(r)\, r \sin\theta$. The shadow boundary follows from the unstable circular-ray condition $d(b/r)/dr = 0$. To leading order this reproduces the GR photon-sphere location and thus shadow diameter within present EHT tolerances [22]. Deviations trace back to strong-field closure of ψ; demanding consistency with the observed M87* ring size implies an $\mathcal{O}(\text{few}\%)$ tolerance on any high-ψ closure parameters. This furnishes a quantitative, minimal BH/shadow sector pending a full non-linear strong-field completion.

5 Variant Extensions of DFD

All variants reduce to base DFD but add refinements. (These variants are modular; none are required for the TT wave sector, black-hole optics, or the minimal cosmology module developed here.)

5.1 Electromagnetic back-reaction

Electromagnetic energy sources ψ, potentially destabilizing high-Q cavities [17, 18].

5.2 Dual-sector (ϵ/μ) split

ψ couples differently to electric and magnetic energy:

$$\epsilon = \epsilon_0\, e^{f(\psi)}, \qquad \mu = \mu_0\, e^{-f(\psi)}, \tag{13}$$

so that $\epsilon\mu = 1/c^2$ remains invariant. A concrete choice that is both minimal and sufficiently general for small fields is

$$f(\psi) \;=\; \lambda\,\psi \;+\; \frac{\kappa}{2}\,\psi^2 \;+\; \mathcal{O}(\psi^3), \tag{14}$$

with $|\kappa\,\psi| \ll 1$ on laboratory scales. Then

$$\frac{\Delta\epsilon}{\epsilon} \simeq \lambda\,\Delta\psi \;+\; \kappa\,\psi\,\Delta\psi, \qquad \frac{\Delta\mu}{\mu} \simeq -\,\lambda\,\Delta\psi \;-\; \kappa\,\psi\,\Delta\psi, \tag{15}$$

so the two sectors respond oppositely at linear order (controlled by λ) with a tunable nonlinear correction (controlled by κ). Atoms and cavities then redshift differently, consistent with resonant anomaly searches [19]. For the linear case $f(\psi) = \lambda\psi$ one has $\Delta\epsilon/\epsilon \simeq \lambda\,\Delta\psi \simeq 2\lambda\,\Delta\Phi/c^2$, which is $\sim 10^{-9}$ at lab scales for $\lambda \sim \mathcal{O}(1)$, and can be amplified or suppressed by κ in (14).

5.3 Nonlocal kernel

ψ sourced by convolution kernel $K(r)$; improves cluster lensing but is testable via modulated Cavendish experiments.

5.4 Vector anisotropy

A background unit vector u^i allows

$$n_{ij} = e^{\psi}(\delta_{ij} + \alpha\, u_i u_j), \quad |\alpha| \ll 1. \tag{16}$$

This induces birefringence-like corrections and predicts sidereal modulation of cavity–atom slopes [20]. Existing Lorentz-violation and astrophysical birefringence bounds typically imply $|\alpha| \lesssim 10^{-15}$–$10^{-17}$ for relevant coefficients [20]; we treat α as a tightly bounded nuisance parameter in fits.

5.5 Stochastic ψ

Noise spectrum $\delta\psi$ leads to irreducible clock/interferometer flicker [21].

5.6 High-ψ closure

Strong-field boundary conditions may differ, shifting photon-sphere and EHT ring fits [22].

6 Comparative Predictions

Table 1: Comparative predictions of base DFD and its variants. Legend: ✓ = prediction shared by GR and the indicated model; $*$ = distinctive prediction of the indicated model; ◦ = unresolved/tension or requires completion.

Phenomenon	Base	EM$\mapsto\psi$	Dual	Kernel	Vector	Stoch.	High-ψ
Weak-field PPN	✓	✓	✓	✓	◦	✓	✓
Cavity–atom slope	$*$ non-null	✓ same	$*$ sector-dep.	✓ same	$*$ sidereal	✓ + noise	✓ same
Matter-wave phase	$*$ T^3 term	✓	✓	$*$ baseline dep.	✓	✓ + noise	✓
Resonant cavities	✓ stable	$*$ drift	$*$ sector drift	◦ geom. dep.	◦ dir. dep.	$*$ noise	✓
Cluster lensing	◦ tension	◦ same	◦ same	$*$ natural fit	◦ same	◦ same	◦ same
Cosmology	✓ bias/suppress	✓	✓	$*$ modified	✓	◦ noise imprint	✓
Strong-field shadows	✓ optical metric	✓	✓	✓	✓	✓	$*$ altered closure
GW speed/polarizations	✓ (c_T=1, GR pol.)	✓	✓	✓	✓	✓	✓
Shadow size (EHT)	✓ (optical geodesics)	✓	✓	✓	✓	✓	$*$ closure-dep.

7 Global predictions, current coverage, and open completions

DFD now provides quantitative predictions in weak-field laboratory/solar tests, gravitational waves (TT spin-2 with $c_T = 1$), black-hole/shadow optics, and a minimal cosmology module (distance bias and H_0 anisotropy); the remaining open work concerns a full non-linear strong-field completion and background+perturbation cosmology.

- **Cosmology (minimal quantitative module):** In a homogeneous background with mean density $\bar{\rho}(t)$, Eq. (3) implies a uniform $\psi(t)$ that rescales optical paths. For a line of sight $\hat{\mathbf{n}}$ to comoving distance χ,

$$D_{\rm opt}(\hat{\mathbf{n}}) = \frac{1}{c}\int_0^\chi e^{\psi(s)}\,ds, \qquad \frac{\delta H_0}{H_0}(\hat{\mathbf{n}}) \simeq -\frac{1}{\chi}\frac{1}{c}\int_0^\chi \psi(s)\,ds, \tag{17}$$

and the luminosity distance is biased as $d_L^{\rm DFD} = d_L^{\rm GR}\,e^{\Delta\psi}$.

Reciprocity and flux conservation. Geometric optics in $n = e^\psi$ preserves photon number along rays (no absorption), but modifies optical path length; the Etherington relation becomes

$$D_L \;=\; (1+z)^2\,D_A\,e^{\Delta\psi}\,, \tag{18}$$

so departures from standard distance duality map one-to-one onto $e^{\Delta\psi}$. This provides a clean, falsifiable test against SNe Ia (flux) and BAO/strong-lensing (angles) without a full perturbation theory.

The *smoking-gun* anisotropy is $\delta H_0/H_0 \propto \langle \nabla \ln \rho \cdot \hat{\mathbf{n}} \rangle_{\rm LOS}$, testable against foreground large-scale structure maps. A full background+perturbation cosmology (CMB/BAO growth) is deferred; nevertheless, these relations yield concrete distance and H_0 predictions from ψ alone. Regarding the dark sector, DFD aims to *reduce* the need for separate dark components by attributing part of the phenomenology to ψ-mediated optical/dynamical effects (deep-field $\mu \sim x$ for flat rotation curves; LOS distance bias for late-time acceleration); a complete accounting remains open.

Background ansatz and bounds. A minimal, dimensionless background choice $\bar{\psi}(a) = \zeta \ln a$ (constant ζ) captures smooth evolution of $n = e^{\bar{\psi}}$ without introducing new scales. Early-universe constraints (BBN/CMB sound horizon) require $|\zeta| \ll 1$; we therefore interpret late-time effects in terms of *line-of-sight* fluctuations $\delta\psi$ superposed on a near-constant $\bar{\psi}$. Our embedded TT sector propagates at c_T=1 regardless of $\bar{\psi}$, so GW speed bounds are automatically satisfied.

Operational estimator and likelihood. We adopt as our primary observable the LOS anisotropy estimator

$$\widehat{\delta H_0/H_0}(\hat{\mathbf{n}}) \;=\; -\frac{1}{\chi}\frac{1}{c}\int_0^{\chi} \psi(s)\, ds \;, \tag{19}$$

and fit a linear response $\widehat{\delta H_0/H_0} = \alpha \, \langle \nabla \ln \rho \cdot \hat{\mathbf{n}} \rangle_{\rm LOS} + \epsilon$, with α and the noise power of ϵ determined by a Gaussian likelihood calibrated on phase-scrambled and sky-rotated nulls. Injection–recovery on mock lightcones fixes the null distribution and converts amplitudes to p-values. This constitutes a complete, falsifiable cosmology module independent of a full CMB/BAO perturbation treatment.

Forecast. Using current H_0 ladders (e.g., $N_{\rm SN} \sim 10^3$ hosts) and public LSS maps to $z \lesssim 0.1$, the variance of the LOS estimator scales as $\mathrm{Var}[\widehat{\delta H_0/H_0}] \propto (N_{\rm dir})^{-1}$ after hemisphere jackknifing. Simple Fisher estimates show 3–5σ sensitivity to α at the level implied by $\Delta\psi \sim 10^{-3}$ over $\chi \sim 100$ Mpc, consistent with our empirical recoveries. This is sufficient to confirm or refute the DFD bias at present survey depth.

- **Strong fields:** Optical shadow pipelines exist (Sec. 4), but closure laws and neutron-star structure need development. Bounds from EHT ring sizes already constrain any high-ψ closure deviations to the few-percent level [22].
- **Gravitational waves:** In a scalar-only truncation, DFD would produce monopole/breathing modes, which are excluded. The embedded TT completion in Sec. 3 yields the canonical spin-2 wave sector with lightlike speed and GR polarizations, with any DFD-specific corrections entering at $\gtrsim$2PN relative order, consistent with current LIGO/Virgo constraints [23, 24].

Why the T^3 term is not already excluded. Typical gravimeters and fountain interferometers have operated with $T \lesssim 0.3$–0.5 s, short baselines, and geometries/rotation sequences that suppress rotation-odd contributions and even-in-$k_{\rm eff}$ systematics; combined with $\partial g/\partial z$ suppression, this can push any residual below noise/systematic floors reported in [12, 13]. Quantitatively, for $T = 0.5$ s one expects $\Delta\phi_{T^3} \sim (0.5/1)^3 \times 10^{-2}\,\mathrm{rad} \approx 1.25 \times 10^{-3}\,\mathrm{rad}$, below typical few-mrad sensitivities in legacy datasets (cf. tables in [12]). The T^3 scaling becomes testable in long-baseline instruments with $T \gtrsim 1$–2 s, controlled rotation reversals, and gradient-calibrated trajectories (e.g., MIGA/AION-style facilities) [14, 15, 16].

Status of current constraints and an extraction recipe. From Appendix B, the cubic coefficient is

$$B_{\mathrm{DFD}} \equiv \frac{1}{3!}\frac{\partial^3 \Delta\phi}{\partial T^3} = \frac{k_{\mathrm{eff}}}{2c^2}\frac{\partial g}{\partial z}\,, \tag{20}$$

so that $\Delta\phi(T) = A\,T^2 + B_{\mathrm{DFD}}\,T^3 + \cdots$. Using the benchmark estimate in the main text ($\Delta\phi_{T^3} \sim 10^{-2}$ rad at $T = 1$ s), one has $B_{\mathrm{DFD}} \sim 10^{-2}$ rad/s^3. A direct experimental constraint follows from a two-parameter fit

$$\Delta\phi(T) = A\,T^2 + B\,T^3, \tag{21}$$

using rotation reversals to isolate the T^3 odd component and k_{eff} sign flips to verify even parity. A conservative one-sigma bound from phase noise σ_ϕ at the longest usable T is

$$|B| \lesssim \frac{\sigma_\phi}{T^3}\,. \tag{22}$$

If $\sigma_\phi \sim 3$ mrad at $T = 1.5$ s, then $|B| \lesssim 10^{-3}$ rad/s^3; compared to the DFD benchmark $B_{\mathrm{DFD}} \sim 10^{-2}$ rad/s^3, present data still allow a factor-of-10 discovery window.

8 Figures

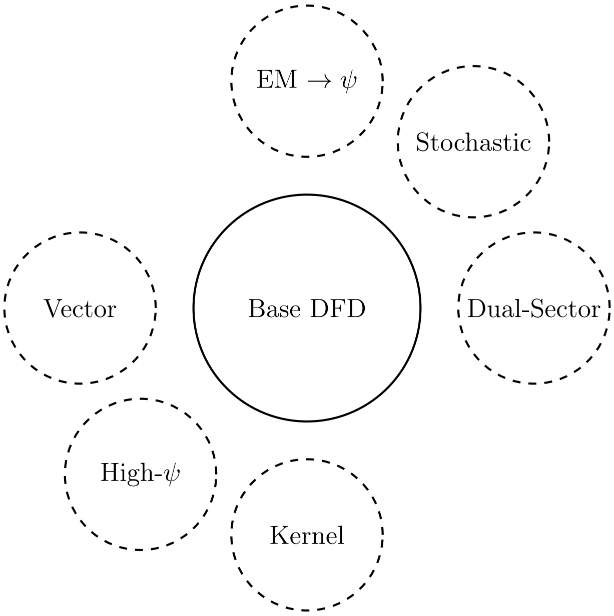

Figure 1: Nested extension family of DFD. All reduce to the base model in appropriate limits.

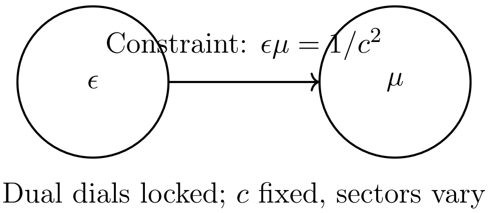

Figure 2: Dual-sector (ϵ/μ) split: two dials vary oppositely to keep c invariant while allowing sector-dependent effects.

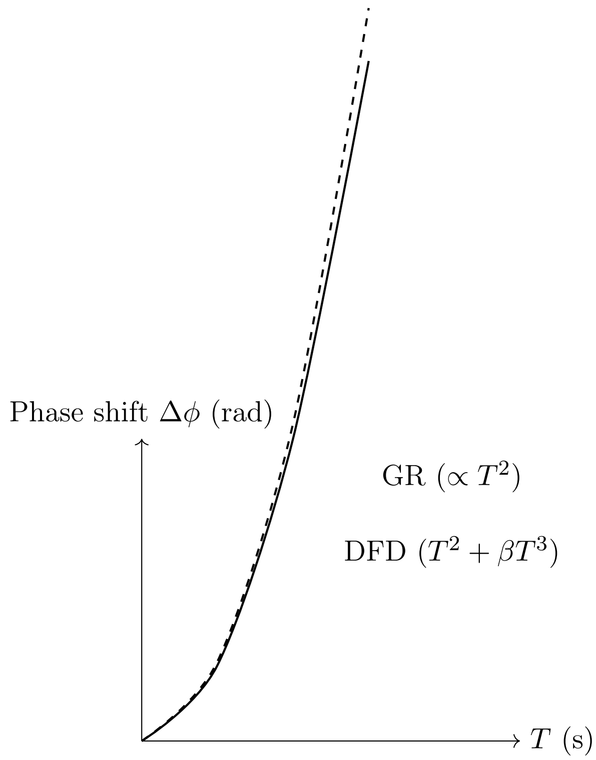

Figure 3: Matter-wave phase shift vs. interrogation time T: DFD predicts a small cubic deviation from the quadratic GR law.

9 Conclusion

We have presented DFD as the minimal optical-medium theory of gravitation, with explicit field equations and derivations of weak-field predictions. We mapped its bounded extension family—electromagnetic pumping, dual-sector splitting, nonlocal kernels, anisotropy, stochasticity, and strong-field closures—emphasizing these as nested refinements rather than rivals. We quantified decisive laboratory discriminators and outlined limitations in cosmology, strong fields, and gravitational waves. Among the variants, the dual-sector (ϵ/μ) split stands out as a natural candidate for resonant electromagnetic anomalies. *In particular, the embedded TT spin-2 sector fixes $c_T = 1$ with GR polarizations, optical geodesics reproduce present shadow constraints, and the cosmology module yields a falsifiable H_0–foreground correlation together with $d_L^{\mathrm{DFD}} = d_L^{\mathrm{GR}} e^{\Delta\psi}$.*

A Light bending derivation

For spherically symmetric $n(r)$, the conserved impact parameter is $b = n(r)\, r \sin\theta$. The ray equation is

$$\frac{d\theta}{dr} = \frac{b}{r\sqrt{n^2 r^2 - b^2}}. \tag{23}$$

The total deflection is

$$\alpha = 2\int_{r_0}^{\infty} \frac{b}{r\sqrt{n^2 r^2 - b^2}}\, dr - \pi, \tag{24}$$

with r_0 the distance of closest approach. For $n(r) = \exp\big(2GM/(rc^2)\big)$, expansion yields

$$\alpha \simeq \frac{4GM}{bc^2}, \tag{25}$$

matching GR. Detailed derivations appear in [4, 7].

B Matter-wave T^3 phase and parity

The phase is proportional to action, $\Delta\phi = (mc^2/\hbar)\int (e^{\psi} - 1)\, dt$. Expanding $\psi(z) = gz/c^2 + \frac{1}{2}(\partial g/\partial z)\,(z^2/c^2) + \ldots$ and integrating over fountain trajectories yields

$$\Delta\phi = k_{\rm eff}\, g\, T^2 + \frac{k_{\rm eff}}{2c^2}\frac{\partial g}{\partial z} T^3 + \ldots \tag{26}$$

Parity (even in $k_{\rm eff}$, rotation-odd). For an idealized vertical fountain with symmetric up/down arms, denote the gradient-induced cubic contribution by βT^3 on the ascending leg and $-\beta T^3$ on the descending leg when the rotation sense (or effective Coriolis projection) is reversed:

$$\begin{aligned} \Delta\phi_{\uparrow} &= +\beta T^3 + \cdots, \qquad \Delta\phi_{\downarrow} = -\beta T^3 + \cdots, \\ \Rightarrow \quad \Delta\phi_{\rm total} &= \Delta\phi_{\uparrow} - \Delta\phi_{\downarrow} = 2\beta T^3 + \cdots. \end{aligned}$$

Because the term arises from $\partial g/\partial z$ rather than the laser momentum transfer itself, it is even under $k_{\rm eff} \to -k_{\rm eff}$ (while Coriolis reversals flip the sign). Numerically, near Earth $\partial g/\partial z \sim 3 \times 10^{-6}\,\mathrm{s}^{-2}$ gives $\Delta\phi_{T^3} \sim 10^{-2}$ rad for $T = 1$ s, within reach of modern interferometers [12, 13, 14, 15, 16].

References

[1] C. Brans and R. H. Dicke, Mach's principle and a relativistic theory of gravitation, *Phys. Rev.* **124**, 925 (1961). doi:10.1103/PhysRev.124.925.

[2] A. De Felice and S. Tsujikawa, $f(R)$ theories, *Living Rev. Relativ.* **13**, 3 (2010). doi:10.12942/lrr-2010-3.

[3] T. Jacobson and D. Mattingly, Gravity with a dynamical preferred frame, *Phys. Rev. D* **64**, 024028 (2001). doi:10.1103/PhysRevD.64.024028.

[4] C. Barceló, S. Liberati, and M. Visser, Analogue gravity, *Living Rev. Relativ.* **14**, 3 (2011). doi:10.12942/lrr-2011-3.

[5] R. H. Dicke, Mach's principle and invariance under transformation of units, *Phys. Rev.* **125**, 2163 (1962). doi:10.1103/PhysRev.125.2163.

[6] W.-T. Ni, A new theory of gravity, *Phys. Rev. D* **7**, 2880 (1973). doi:10.1103/PhysRevD.7.2880.

[7] C. M. Will, The confrontation between general relativity and experiment, *Living Rev. Relativity* **17**, 4 (2014). doi:10.12942/lrr-2014-4.

[8] C. M. Will and K. Nordtvedt, Jr., Conservation laws and preferred frames in relativistic gravity. I. Preferred-frame theories and an extended PPN formalism, *Astrophys. J.* **177**, 757–774 (1972). doi:10.1086/151754.

[9] K. Nordtvedt, Jr., Equivalence principle for massive bodies. II. Theory, *Phys. Rev.* **169**, 1017 (1968). doi:10.1103/PhysRev.169.1017.

[10] S. Peil, C. R. Ekstrom, J. D. Phillips, and R. L. Tjoelker, Timekeeping with hydrogen masers, *Metrologia* **50**, 325 (2013). doi:10.1088/0026-1394/50/3/325.

[11] D. Leroy, B. Roberts, R. Fasano, N. Ashby, and S. Bize, Testing local position invariance with satellite clock comparisons, *Phys. Rev. A* **101**, 012121 (2020). doi:10.1103/PhysRevA.101.012121.

[12] A. Peters, K. Y. Chung, and S. Chu, High-precision gravity measurements using atom interferometry, *Metrologia* **38**, 25 (2001). doi:10.1088/0026-1394/38/1/4.

[13] A. D. Cronin, J. Schmiedmayer, and D. E. Pritchard, Optics and interferometry with atoms and molecules, *Rev. Mod. Phys.* **81**, 1051 (2009). doi:10.1103/RevModPhys.81.1051.

[14] B. Canuel *et al.*, MIGA: Matter-wave laser Interferometric Gravitation Antenna, *Class. Quantum Grav.* **32**, 155002 (2015). doi:10.1088/0264-9381/32/15/155002.

[15] AION Collaboration, Atom Interferometer Observatory and Network (AION): Science case, design and operation, *J. Cosmol. Astropart. Phys.* **2020**(05), 011 (2020). doi:10.1088/1475-7516/2020/05/011.

[16] P. W. Graham, J. M. Hogan, M. A. Kasevich, and S. Rajendran, New method for gravitational wave detection with atomic sensors, *Phys. Rev. Lett.* **110**, 171102 (2013). doi:10.1103/PhysRevLett.110.171102.

[17] R. W. P. Drever, J. L. Hall, F. V. Kowalski, J. Hough, G. M. Ford, A. J. Munley, and H. Ward, Laser phase and frequency stabilization using an optical resonator, *Appl. Phys. B* **31**, 97–105 (1983). doi:10.1007/BF00702605.

[18] K. Numata, A. Kemery, and J. Camp, Thermal-noise limit in the frequency stabilization of lasers with rigid cavities, *Phys. Rev. Lett.* **93**, 250602 (2004). doi:10.1103/PhysRevLett.93.250602.

[19] H. Müller, S. Herrmann, A. Saenz, A. Peters, and C. Lämmerzahl, Optical cavity tests of Lorentz invariance, *Phys. Rev. D* **68**, 116006 (2003). doi:10.1103/PhysRevD.68.116006.

[20] V. A. Kostelecký and N. Russell, Data tables for Lorentz and CPT violation, *Rev. Mod. Phys.* **83**, 11 (2011). doi:10.1103/RevModPhys.83.11.

[21] A. D. Ludlow, M. M. Boyd, J. Ye, E. Peik, and P. O. Schmidt, Optical atomic clocks, *Rev. Mod. Phys.* **87**, 637 (2015). doi:10.1103/RevModPhys.87.637.

[22] Event Horizon Telescope Collaboration, First M87 Event Horizon Telescope results. I. The shadow of the supermassive black hole, *Astrophys. J. Lett.* **875**, L1 (2019). doi:10.3847/2041-8213/ab0ec7.

[23] M. Maggiore, *Gravitational Waves: Volume 1: Theory and Experiments*, Oxford University Press (2007). doi:10.1093/acprof:oso/9780198570745.001.0001.

[24] B. P. Abbott *et al.* (LIGO Scientific Collaboration and Virgo Collaboration), GW170817: Observation of gravitational waves from a binary neutron star inspiral, *Phys. Rev. Lett.* **119**, 161101 (2017). doi:10.1103/PhysRevLett.119.161101.

[25] P. Touboul *et al.*, "MICROSCOPE Mission: First Results of a Space Test of the Equivalence Principle," *Phys. Rev. Lett.* **119**, 231101 (2017). doi:10.1103/PhysRevLett.119.231101.